JACS
JOURNAL OF THE AMERICAN CHEMICAL SOCIETY

Article

pubs.acs.org/JACS

Heterogeneous Sensitization of Metal–Organic Framework Driven Metal@Metal Oxide Complex Catalysts on an Oxide Nanofiber Scaffold Toward Superior Gas Sensors

Won-Tae Koo,[†] Seon-Jin Choi,[†,§] Sang-Joon Kim,[†] Ji-Soo Jang,[†] Harry L. Tuller,[‡] and Il-Doo Kim*[,†]

[†]Department of Materials Science and Engineering and [§]Applied Science Research Institute, Korea Advanced Institute of Science and Technology, Daejeon 34141, Republic of Korea

[‡]Department of Materials Science and Engineering, Massachusetts Institute of Technology, Cambridge, Massachusetts 02139, United States

Supporting Information

ABSTRACT: We report on the heterogeneous sensitization of metal–organic framework (MOF)-driven metal-embedded metal oxide (M@MO) complex catalysts onto semiconductor metal oxide (SMO) nanofibers (NFs) via electrospinning for markedly enhanced chemical gas sensing. ZIF-8-derived Pd-loaded ZnO nanocubes (Pd@ZnO) were sensitized on both the interior and the exterior of WO_3 NFs, resulting in the formation of multiheterojunction Pd–ZnO and ZnO–WO_3 interfaces. The Pd@ZnO loaded WO_3 NFs were found to exhibit unparalleled toluene sensitivity (R_{air}/R_{gas} = 4.37 to 100 ppb), fast gas response speed (~20 s) and superior cross-selectivity against other interfering gases. These results demonstrate that MOF-derived M@MO complex catalysts can be functionalized within an electrospun nanofiber scaffold, thereby creating multiheterojunctions, essential for improving catalytic sensor sensitization.

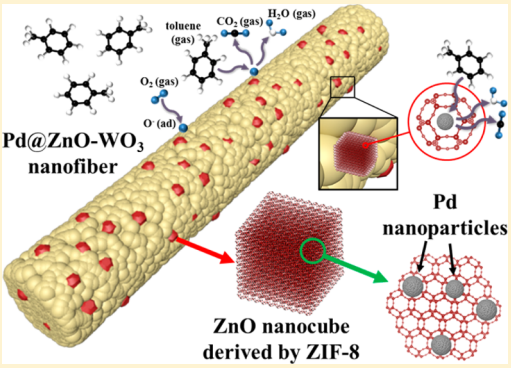

INTRODUCTION

Metal–organic frameworks (MOFs) have received much recent attention due to their distinctive features such as exceptionally high surface area, ultrahigh porosity, and diverse structures.[1] This has stimulated research on a variety of potential MOF applications, including gas storage,[2] catalysis,[3] sensors,[4] and drug delivery.[5] A particularly noteworthy feature of MOFs is their ability to encapsulate noble metal nanoparticles (NPs), such as Pt and Pd, within their cavities (metal@MOF).[6] Hermes et al.[6a] first reported metal@MOF by releasing the metal atoms from the precursors using metal organic chemical vapor deposition for infiltrating metal atoms into MOFs. Lu et al.[6b] used surfactants for the controlled encapsulation of noble metal catalysts such as Au, and Pt into zeolite imidazole frameworks (ZIF-8). Jiang et al.[6c] succeeded in encapsulating core–shell NPs into ZIF-8 by sequential deposition and reduction of metal precursors. Because the catalyst NPs are embedded in the cavity of MOFs, the sizes of the NPs are limited to a few nanometers in dimension. Thus far, a number of studies have proposed utilizing metal@MOF structures as catalysts.[7] K. M. Choi et al.[7a] synthesized Pt-embedded UiO-66 and investigated their catalytic activities in the gas-phase conversion of methylcyclopentane. J. M. Yan et al.[7b] reported AuPd, MnO_x, ZIF-8, and graphene composite catalysts for hydrogen production. However, these approaches suffer from the relatively poor chemical stability of MOFs. In particular, the MOF structure is unstable at high temperatures due to thermal instability of organic linkers within the MOFs.

Here, we propose a new catalyst loading method using metal@MOF for ultrahigh performance chemical gas sensors. To achieve high performance chemi-resistive gas sensors, catalytic sensitization should be optimized on the surface of semiconductor metal oxides (SMOs). Conventionally, noble metal catalysts such as Pd, Pt, and Au have generally been sensitized on WO_3, SnO_2, and ZnO for high performance gas sensors.[8] Although the functionalization of nanoscale noble metal catalysts can dramatically enhance the sensing properties of chemi-resistive gas sensors, catalyst agglomeration results in sensing performance degradation.[8b] Difficulty in achieving uniform distributions of ultrasmall noble metal catalysts on sensing materials is therefore one of the biggest obstacles in developing superior gas sensors. Achieving highly accurate detection of target analytes in exhaled breath also remains a major challenge,[8c] given that trace concentrations in the range of 10–100 ppb level in high humidity need be detected for disease diagnosis. High humidity atmospheres, essential for reliable breath analysis, create particularly harsh environments for the detection of target gases.[9] To achieve highly sensitive and selective detection of ultralow concentrations of analytes at high humidity, a new type of heterogeneous complex catalyst

Received: September 1, 2016
Published: September 19, 2016

DOI: 10.1021/jacs.6b09167
J. Am. Chem. Soc. 2016, 138, 13431–13437

needs to be explored. In this work, we propose heterogeneous sensitization of ultrasmall noble metal catalyst loaded metal oxide (M@MO) applied to SMO nanofibers (NFs) during electrospinning. The MOF templated catalytic NPs are functionalized on SMO NFs through electrospinning followed by calcination. During calcination, metal ion species, comprised of metal@MOFs, are oxidized, leading to the formation of a metal oxide scaffold, while catalyst NPs remain embedded within the MOFs. The calcined metal oxide scaffold can serve as the host backbone for the uniform distribution of catalyst NPs within the oxide cavity. The M@MO then act as synergistic catalysts by forming additional heterojunctions between the metal oxide backbone and the SMO NFs. In this manner, the ultrasmall and highly porous MOF-driven M@MO complex catalysts are fully utilized and thereby maximize the catalytic reaction. In addition, the functionalization of M@MO complex catalysts onto the one-dimensional (1-D) NFs via electrospinning, a facile and versatile method for synthesizing 1-D nanostructures, is a very efficient and robust loading route, providing large surface area, and high gas accessibility as required for high performance chemical sensors.[10] Furthermore, double heterojunctions in M@MO loaded 1-D NFs significantly enhance the chemical sensing performance. Previously, pure MOF (ZIF-8, MIL-101), combined with electrospinning, was reported.[11] Metal@MOF templates have, however, never been adopted for functionalization of a SMO NF scaffold. Furthermore, the superior chemical sensing response of electrospun oxide NFs functionalized by MOF-derived M@MO complex catalysts has never been reported.

RESULTS AND DISCUSSION

In this work, we prepared Pd-loaded ZnO particles as MOF driven M@MO complex catalysts, that are further functionalized onto WO_3 NFs (hereafter, Pd@ZnO-WO_3 NFs). The Pd@ZnO was synthesized by encapsulating Pd in the cavity of ZIF-8 (Pd@ZIF-8) templates, followed by subsequent calcination. On the basis of the previous studies, Pd NPs functionalized on ZnO or WO_3 can promote toluene sensing.[12] Therefore, we expect that the toluene sensing properties of Pd@ZnO-WO_3 NFs could be synergistically enhanced by the ultrasmall and well-dispersed Pd NPs accompanied by heterojunctions introduced by the Pd@ZnO complex catalysts.

Figure 1a illustrates the synthetic route of highly dispersed Pd NPs, embedded in the cavity of ZIF-8 by reduction of Pd^{2+} ions.[6c] ZIF-8 consists of Zn atoms with the 2-methylimidazole organic framework. The inner cavity dimensions of the ZIF-8 are on the order of ~11.6 Å.[13] Pd^{2+} ions can diffuse into the ZIF-8 cavity by infiltration in solution. Following reduction by sodium borohydride ($NaBH_4$), Pd^{2+} ions are transformed into metallic Pd NPs. The prepared pristine ZIF-8 exhibited 3-D cubic morphologies with diameters in the range of 50−200 nm (Figure S1a of the Supporting Information, SI). The powder X-ray diffraction (PXRD) analysis was matched with the simulated PXRD data of ZIF-8, and the microporous structure of ZIF-8 was confirmed by N_2 adsorption/desorption isotherms at 77K (Figure S2b). After Pd NP encapsulation in ZIF-8, a high concentration of Pd NPs was well-distributed within the cavities of ZIF-8 (Figures 1b and S1b) without aggregation. A high resolution transmission electron microscopy (HRTEM) image revealed the Pd (111) crystal plane corresponding to the interplanar distance of 2.25 Å (Figure 1c). Moreover, the dimensions of the Pd NPs were found to be 2−3 nm. Although the sizes of the Pd NPs were larger than the cavity diameter, the

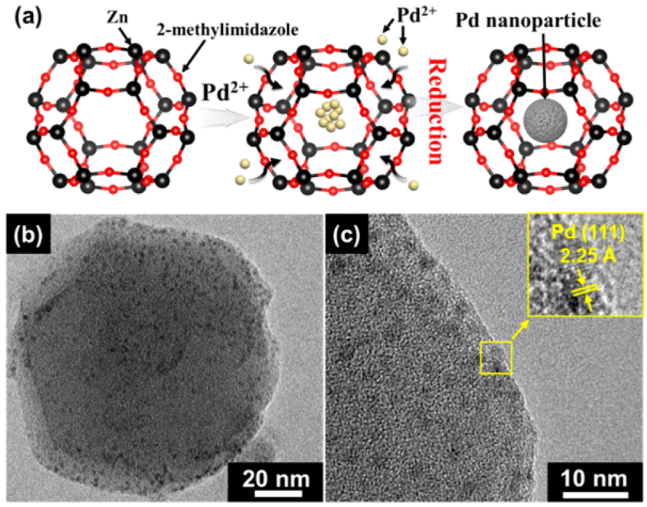

Figure 1. (a) Schematic illustration of Pd NP encapsulation in the cavity of ZIF-8, (b) TEM image of Pd@ZIF-8, and (c) HRTEM image of Pd@ZIF-8.

XRD patterns and pore size distribution of Pd@ZIF-8 were identical with those of pristine ZIF-8 (Figure S2). In addition, the N_2 adsorption/desorption isotherms of Pd@ZIF-8 exhibited a microporous structure. However, the Pd-related peaks were not observed in the PXRD analysis, and the decreased gravimetric Brunauer−Emmett−Teller (BET) surface area of Pd@ZIF-8 was displayed in the N_2 uptake isotherm. These results are consistent with previous studies on metal@ZIF-8.[6b,d] The porous structure of ZIF-8 did not change during metal encapsulation, and the weak intensity of Pd can be attributed to the encapsulation by ZIF-8, and the small size of Pd NPs. In addition, the decrease of BET surface area was attributed to the mass contribution of nonporous Pd NPs in Pd@ZIF-8. The synthesized Pd@ZIF-8 particles were directly utilized as templates for the multiheterogeneous functionalization of Pd@ZnO complex catalysts on WO_3 NF scaffolds.

Pd@ZnO−WO_3 NFs were finally achieved by electrospinning (Figure 2a) of a composite solution comprising Pd@ZIF-8, polyvinylpyrrolidone (PVP), and ammonium metatungstate hydrate (AMH, $[(NH_4)_6H_2W_{12}O_{40}{\cdot}xH_2O]$), with subsequent calcination in air. During calcination, the ZIF-8 was oxidized to a ZnO framework and the Pd@ZnO particles were tightly immobilized onto the porous WO_3 NFs due to the thermal decomposition of the PVP matrix and the crystallization of WO_3. The burning-out of the organic linkers comprising the MOF resulted in the formation of mesopores within the WO_3 NFs. As indicated in Figure 2a, the as-spun AMH/PVP NFs, including Pd@ZIF-8 particles, showed a nonwoven 1-D nanostructure with diameters in the range of 500−950 nm, with micrograph in Figure 2b showing ZIF-8 cubes on the surface of the composite NFs (yellow arrows in Figure 2b). Most of the Pd@ZIF-8 particles were embedded in the AMH/PVP NFs, and some of them were observed on the surface of composite NFs (Figure 2c). In addition, the HRTEM image clearly exhibited the (111) crystal plane of Pd and the well-dispersed Pd NPs in the composite NFs (Figure 2d). Moreover, the results of energy dispersive X-ray spectroscopy (EDS) elemental mapping using TEM confirmed that the Pd@ZIF-8 were well-distributed in the composite NFs (Figure S3). After calcination, the NF diameter reduced to 400−850 nm. The pure ZIF-8 derived ZnO (reference sample) or the Pd@

DOI: 10.1021/jacs.6b09167
J. Am. Chem. Soc. 2016, 138, 13431−13437

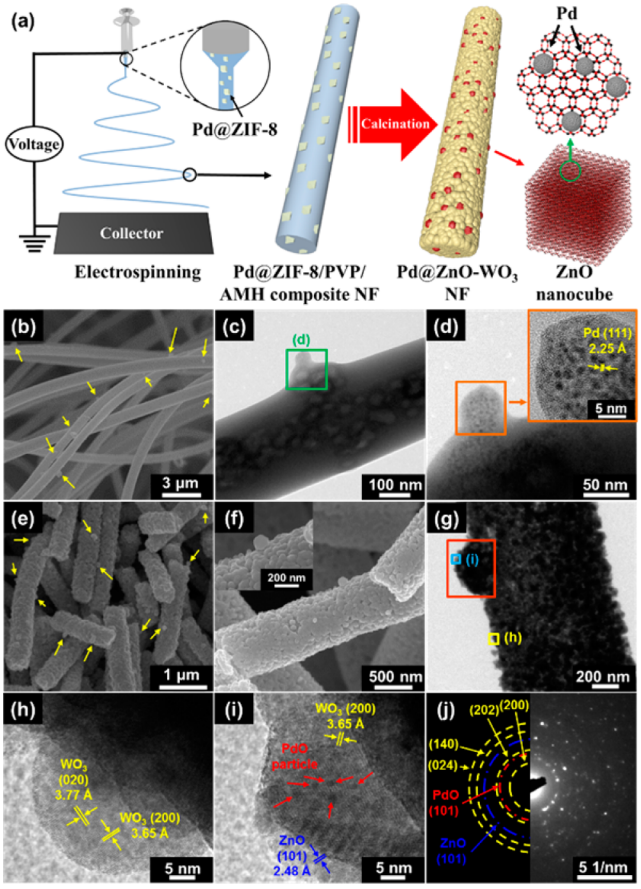

Figure 2. (a) Schematic illustration of synthetic process for the Pd@ZnO−WO_3 NFs, (b) Scanning electron microscopy (SEM) image of as-spun AMH/PVP/Pd@ZIF-8 NFs, (c,d) TEM images of AMH/PVP/Pd@ZIF-8 NFs and (inset) HRTEM image (e,f) SEM images of Pd@ZnO−WO_3 NFs and (inset) magnified image of surface, (g) TEM image of Pd@ZnO−WO_3 NF, (h,i) HRTEM images of Pd@ZnO−WO_3 NF, and (j) SAED pattern of Pd@ZnO−WO_3 NFs.

ZnO decorated both the inside and outside of the WO_3 NFs (yellow arrows in Figures S4a and 2e). Most of the Pd@ZnO particles on the surface of WO_3 NFs are not clearly distinguished from WO_3 crystals (Figure 2f). To compare with the Pd@ZnO-WO_3 NFs, we also synthesized pristine WO_3 NFs as control samples. The as-spun and calcined composite NFs exhibited both 1-D structures (Figure S4b,c). The TEM image of Pd@ZnO-WO_3 NFs clearly showed the immobilization of Pd@ZnO nanocube on the NF surface (red box in Figure 2g). The HRTEM image of Pd@ZnO-WO_3 NFs revealed polycrystalline WO_3 NFs with crystal plane of (020) and (200), which correspond to interplanar distances of 3.72 and 3.65 Å, respectively (Figure 2h). Moreover, spherical dark spots were observed on Pd@ZnO−WO_3 NFs, which are presumably PdO NPs (red arrows in Figure 2i). Pd NPs in the composite were oxidized to PdO in air, and reduced to Pd in toluene. The promotion effect of Pd will be discussed later in detail. ZnO was confirmed by noting the presence of (101) crystal planes with interplanar distance of 2.48 Å (Figure 2i). Selective area electron diffraction (SAED) patterns confirmed polycrystalline WO_3 NFs with lattice plane of (200), (202), (140), and (024) (Figure 2j). In addition, the lattice planes of PdO (101) and ZnO (101) were identified in the SAED pattern. The weak intensities of PdO and ZnO lattice planes in the SAED pattern were ascribed to the very low concentrations of PdO and ZnO in Pd@ZnO−WO_3 NFs. To further investigate the existence of PdO and ZnO, we conducted EDS elemental mapping using TEM (Figure S5). The results confirmed that Zn and Pd were well-distributed in the Pd@ZnO-WO_3 NFs, leading to homogeneous sensitization both inside and outside of the WO_3 matrix.

Thermogravimetric analysis (TGA) of AMH/PVP composite NFs and AMH/PVP/ZIF-8 composite NFs were performed to investigate the thermal stability of Pd@ZnO−WO_3 NFs and the decomposition temperature of ZIF-8 (Figure 3). In the

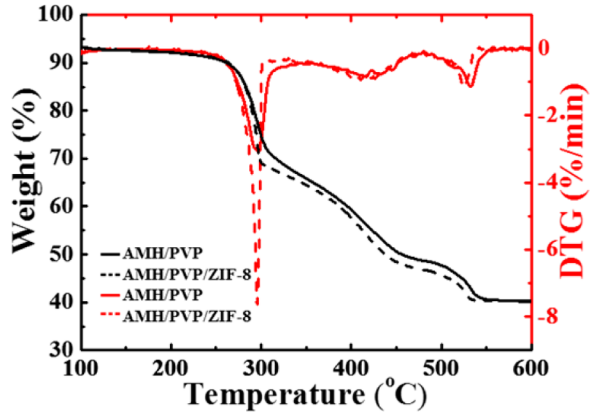

Figure 3. TGA and DTG analysis of the AMH/PVP composite NFs, and AMH/PVP/ZIF-8 composite NFs in the temperature range of 100−600 °C under air atmosphere.

temperature range of 240−310 °C, The NFs' weight sharply decreased due to the decomposition of organic compounds in the starting chemistry of the NFs. Significantly, the weight loss at 300 °C was comparably higher for the AMH/PVP/ZIF-8 NFs relative to that of the PVP/AMH NFs. The organic ligands of ZIF-8 began to decompose in this temperature range, in agreement with a previous study on the thermal stability of ZIF-8.[14] The weight of both composite NFs diminished up to 550 °C. The decomposition of PVP typically occurs in the temperature range of 350−470 °C.[15] In this work, PVP showed a slightly higher burnout temperature (550 °C) due to the interaction between PVP and AMH.[16] The organic compounds in both composite NFs were found to have completely decomposed during calcination for 1 h at 500 °C in air.

The crystal structures and chemical binding states of Pd@ZnO-WO_3 NFs were examined by PXRD and X-ray photoelectron spectroscopy (XPS). The PXRD analysis confirms the monoclinic structure of WO_3 (JCPDS no. 43-1035) and the polycrystalline characteristics of Pd@ZnO−WO_3 NFs (Figure S6). However, characteristic peaks related to ZnO and Pd are not observed in the PXRD analysis because the loading amounts of Pd@ZnO (0.33 wt %) were below the limit of detection. However, XPS analysis clearly revealed that W, Zn, and Pd were completely oxidized to WO_3, ZnO, and PdO due to the high temperature calcination (Figure 4). The XPS analysis using high resolution spectra of Pd@ZnO−WO_3 NFs in the vicinity of W 4*f* peaks exhibited two characteristic peaks of $4f_{5/2}$ and $4f_{7/2}$ at the binding energies of 37.7 and 35.5 eV, respectively, which correspond to the binding energies of W^{6+} states (Figure 4a).[17] Oxygen related peaks showed two oxygen states with dominant O^{2-} state and minor O^- state, located at 530.2 eV for O^{2-} 1*s* and 531.0 eV for O^- 1*s* (Figure 4b).[18] Zn

DOI: 10.1021/jacs.6b09167
J. Am. Chem. Soc. 2016, 138, 13431−13437

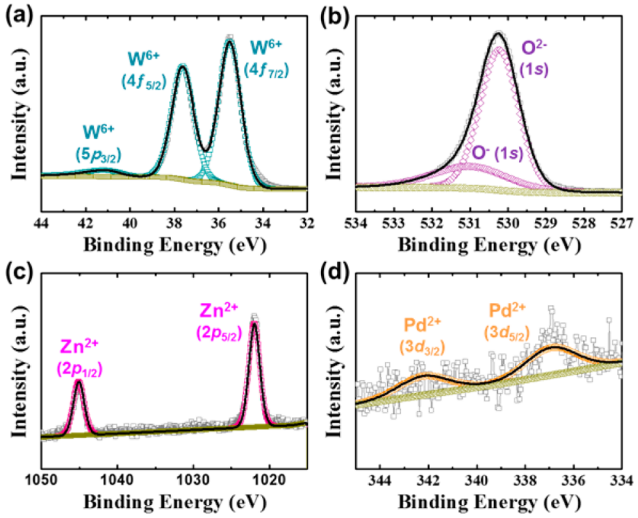

Figure 4. XPS analysis using high resolution spectra of Pd@ZnO−WO_3 NFs in the vicinity of (a) W 4*f*, (b) O 1*s*, (c) Zn 2*p*, and (d) Pd 3*d*.

atoms derived from ZIF-8 were mostly oxidized to Zn^{2+} during the calcination steps, with peaks of $2p_{1/2}$ and $2p_{3/2}$ located at the binding energies of 1345.0 and 1022.0 eV (Figure 4c).[19] Pd atoms encapsulated in the cavity of the ZIF-8 were also oxidized to PdO during the calcination in air ambient. XPS analysis revealed the Pd^{2+} state with peak values at 336.9 eV for $3d_{5/2}$ and 342.2 eV for $3d_{2/3}$ (Figure 4d).[20]

To evaluate the chemical sensing characteristics of Pd@ZnO−WO_3 NFs, the sensing materials were coated onto Au electrode patterned Al_2O_3 substrates. High sensitivity and selectivity toward toluene, well-known as a biomarker in exhaled breath for diagnosis of lung cancer as well as a toxic gas associated with hazardous environments, are highly desired.[21,12b] To confirm the synergistic effect of the Pd@ZnO complex catalyst, Pd NPs with average size of 10 nm were prepared by the conventional polyol process and randomly functionalized on WO_3 NFs (Pd(polyol)−WO_3 NFs) and ZnO−WO_3 NFs (Pd(polyol)−ZnO−WO_3 NFs) by electrospinning (Figure S7). The toluene sensing characteristics of pristine WO_3 NFs, ZnO−WO_3 NFs, Pd(polyol)−WO_3 NFs, Pd(polyol)−ZnO−WO_3 NFs, and Pd@ZnO−WO_3 NFs were all evaluated in a high humidity atmosphere (90% RH), similar to that found in exhaled human breath.

According to previous studies, the sensing response can be affected by the operating temperature, and the catalyst loading.[22] The surface reaction between toluene and chemisorbed oxygen on Pd@ZnO−WO_3 NFs, for example, can be influenced by the operating temperature. In addition, small amounts of catalyst are insufficient to reach full catalytic enhancement. However, excessive amounts of catalysts can cause degradation in gas sensing properties by saturation of catalytic sensitization and catalyst aggregation. The sensor operating temperature (300−450 °C) and loading concentration of the Pd@ZnO complex catalysts (0.034−0.660 wt %) were investigated to identify the optimized sensing response. The molar ratio of Pd/Zn in Pd@ZnO was 1:6.51 in all samples. The largest response was achieved at 350 °C using Pd@ZnO−WO_3 NFs at a doping level of 0.136 wt % Pd@ZnO (Figure S8a,b). The same levels of Pd(polyol) NPs (0.027 wt %) or ZnO (0.109 wt %) sensitized on WO_3 NFs served as controls. Moreover, high humidity can decrease the response to reducing gases in n-type SMO gas sensor, given that water vapor also donates electrons to the SMO by dissociating into hydroxyl groups and thereby lowering the base resistance of the SMO.[20,23] We investigated the effect of high humidity on Pd@ZnO−WO_3 NFs and found that the base resistance of the Pd@ZnO−WO_3 NFs decreased with increasing humidity, and that the response of Pd@ZnO−WO_3 NFs under 90% RH was lower than under dry conditions (Figure S8c,d).

The time dependent response of the sensors, measured at 350 °C, for the concentration range of 1−5 ppm, is shown in Figure 5a. The Pd@ZnO−WO_3 NFs exhibited superior toluene

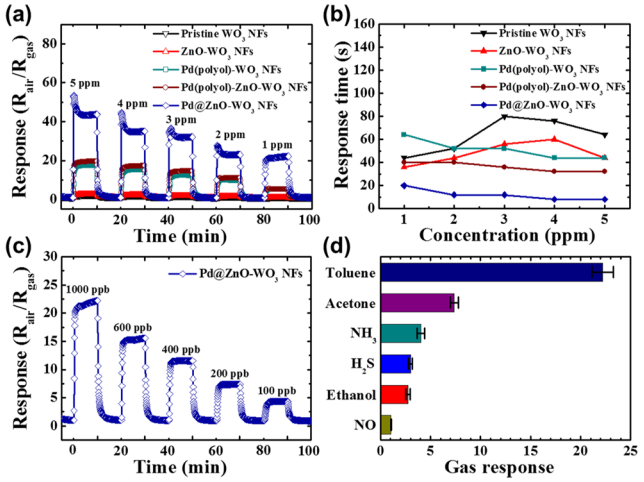

Figure 5. Response characteristics of pristine WO_3, ZnO−WO_3, Pd(polyol)−WO_3, Pd(polyol)−ZnO−WO_3, and Pd@ZnO−WO_3 NFs toward toluene in the concentration range of 1−5 ppm at 350 °C: (a) Dynamic sensing transition, (b) response time evaluation, and (c) detection limit characteristics of the Pd@ZnO−WO_3 NFs toward toluene down to 100 ppb at 350 °C, (d) Selective toluene detection characteristics of the Pd@ZnO−WO_3 NFs with respect to the multiple interfering analytes at a concentration of 1 ppm at 350 °C.

response (R_{air}/R_{gas} = 22.22 to 1 ppm) as compared to pristine WO_3 NFs (R_{air}/R_{gas} = 1.10), ZnO−WO_3 NFs (R_{air}/R_{gas} = 1.16), Pd(polyol)−WO_3 NFs (R_{air}/R_{gas} = 5.31), and Pd(polyol)−ZnO−WO_3 NFs (R_{air}/R_{gas} = 5.47), demonstrating the remarkably improved response achieved by functionalization of the Pd@ZnO complex catalyst onto WO_3 NFs. The response speed of the Pd@ZnO-WO_3 NFs was much faster (<20 s) than for that of pristine WO_3 (44 s), ZnO−WO_3 (36 s), Pd(polyol)−WO_3 NFs (44 s), and Pd(polyol)−ZnO−WO_3 NFs (32 s) (Figure 5b). As evident from Figure 5c, the Pd@ZnO−WO_3 NFs could readily detect 100 ppb of toluene with high sensitivity (R_{air}/R_{gas} = 4.37 at 350 °C). To investigate the selectivity of the Pd@ZnO-sensitized WO_3 NFs sensor, its sensing properties were investigated at 350 °C toward other potential interfering analyte gases such as acetone (CH_3COCH_3), ammonia (NH_3), hydrogen sulfide (H_2S), ethanol (C_2H_5OH), and nitric monoxide (NO) at the 1 ppm level (Figure 5d).[24] The results revealed high sensitivity to toluene (R_{air}/R_{gas} = 22.22), a noticeable response to acetone (R_{air}/R_{gas} = 7.37), but much reduced responses (R_{air}/R_{gas} < 4.03) toward other analytes (NH_3, H_2S, ethanol, and NO). Moreover, high stability was demonstrated by achieving reproducible response to toluene following 7 cycles (R_{air}/R_{gas} = 22.22 ± 1.07 to 1 ppm at 350 °C, Figure S9).

DOI: 10.1021/jacs.6b09167
J. Am. Chem. Soc. 2016, 138, 13431−13437

The mechanism of toluene sensing was previously investigated in several studies.[25] When n-type WO_3 NFs are exposed to air, the oxygen (O_2) molecules are chemically adsorbed in the form of O^-, O^{2-}, and O_2^- on the surface of the WO_3 NFs by attracting electrons from the conduction band of the WO_3. The chemisorbed oxygen species thereby induce the formation of an electron depletion region at the surface of the WO_3. Thereafter, when the WO_3 NFs are exposed to toluene, the resistivity of the WO_3 NFs is decreased due to the surface reaction between toluene and chemisorbed oxygen, producing the byproducts H_2O and CO_2. This results in the back-donation of electrons to the conduction band of the WO_3 ($R_{gas} < R_{air}$).

The enhanced response of the Pd@ZnO−WO_3 NFs toward toluene is interpreted as follows. The formation of ZnO/WO_3 heterojunctions induce energy band bending in both ZnO (band gap =3.37 eV) and WO_3 (band gap =2.7 eV).[26] The UPS analysis identified the work functions of WO_3 NFs (4.85 eV), ZnO powders (5.25 eV), and Pd@ZnO powders (5.30 eV) respectively (Figure S10). Given a difference in work function of 0.4 eV, the respective energy band bending induces electron migration from WO_3 to ZnO (Figure 6). Such electron transfer expands the electron depletion region on WO_3 NFs. The adsorption of oxygen molecules on WO_3 and ZnO further contribute to electron depletion. The base resistance (1.34 MΩ) of ZnO−WO_3 NFs is therefore higher than that (0.39 MΩ) of WO_3 NFs (Figure 6b). Moreover, the sensing characteristics can be enhanced by functionalization of the metal oxides with noble metal catalysts. As an electronic sensitization catalyst, Pd NPs decorated on SMO layers can be oxidized to PdO in air. The p−n heterojunction generated between PdO and ZnO results in reduction of the electron concentration in ZnO by recombination.[27] In addition, the work function of ZnO can increase by PdO loading, as demonstrated in the UPS analysis (Figure S10c). By increasing the difference in work function (0.4 to 0.45 eV), more electrons transfer from WO_3 to Pd@ZnO compared to ZnO/WO_3. Thus, Pd@ZnO−WO_3 NFs exhibit the higher base resistance (9.41 MΩ) in air compared with pristine WO_3 NFs (0.39 MΩ) and ZnO−WO_3 NFs (1.34 MΩ), resulting in the large resistance changes when exposed to toluene (Figure 6b). In addition, the base resistance of Pd@ZnO−WO_3 NFs is higher than that of Pd(polyol)−WO_3 NFs (3.57 MΩ) and Pd(polyol)−ZnO−WO_3 NFs (7.50 MΩ) (Figure 6b). These results revealed that ultrasmall and well-dispersed Pd NPs driven by MOF templates are more effectively sensitized on WO_3 NFs compared with Pd NPs made by the polyol process.

When PdO NPs are then exposed to a reducing gas, e.g., toluene, the PdO is partially reduced to Pd and donates electrons to the ZnO, resulting in effective modulation of the surface depletion layer. To clearly demonstrate the catalytic effect of Pd NPs during sensing measurements, ex situ XPS analysis of Pd@ZnO−WO_3 NFs were carried out. After cyclic measurement of 1 ppm of toluene at 350 °C, the samples were exposed to air and 1 ppm of toluene. In air, Pd NPs existed in the oxidized state (Pd^{2+}) (Figure 6c). However, just after exposure to toluene, the XPS results showed a reduced state of Pd (Pd^0) (Figure 6d). These results confirmed that PdO NPs were partially reduced to Pd during toluene sensing. In addition, more facile surface reactions can be achieved by lowering the activation energy of the reaction between toluene and chemisorbed oxygen: $C_6H_5CH_3$ (gas) + $2O^-$ → $C_6H_5CHO^-$ + H_2O + e^-.[28] These additional electrons, generated by the enhanced surface reaction, contribute to the additional decrease in the resistivity of the sensing materials (Figure 6b). Overall, their features result in the significant enhancement of toluene sensing response.[26b,29] As a consequence, the Pd@ZnO−WO_3 NFs containing multiheterojunctions exhibited superior toluene sensing performances compared with pristine WO_3, ZnO−WO_3, Pd(polyol)-WO_3, and Pd(polyol)−ZnO−WO_3 NFs (Figure 5a,b). Moreover, the mesopores of 20−30 nm formed within the Pd@ZnO−WO_3 NFs further increase surface reactions in comparison with pristine WO_3 NFs (Figure S11). Consequently, the diffusion of toluene can be facilitated in the Pd@ZnO−WO_3 NFs by Knudsen diffusion.[25] In comparison to other studies (Table S1), the toluene sensing performance achieved with M@MO-loaded oxide NFs sensors is markedly enhanced. To the best of our knowledge, these results represent the best toluene sensing performance reported for SMO gas sensors.

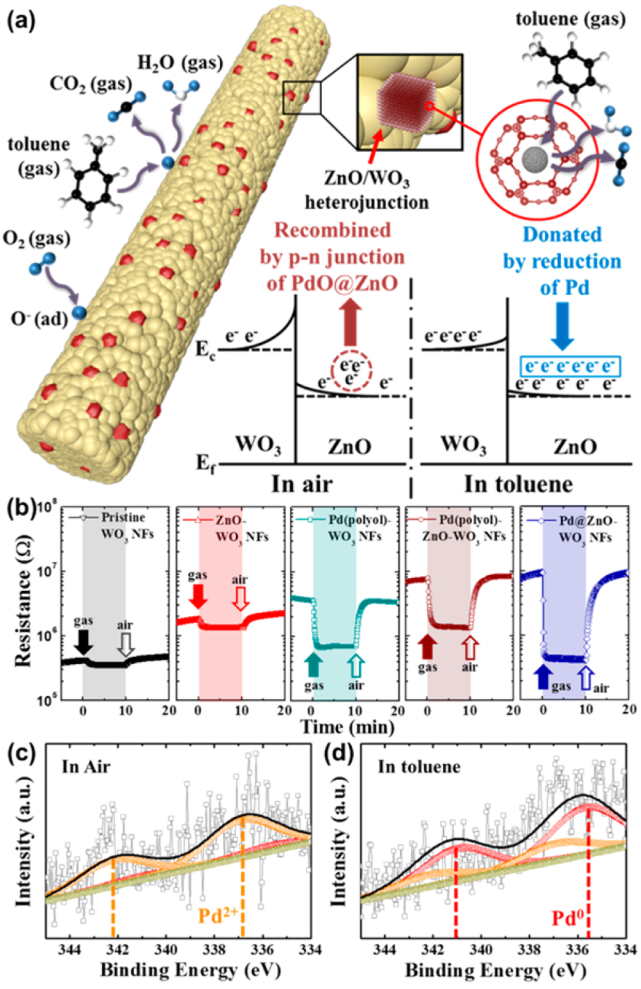

Figure 6. (a) Schematic illustration of toluene sensing mechanism for Pd@ZnO−WO_3 NFs, (b) dynamic resistance transition characteristics toward 1 ppm of toluene at 350 °C, and ex situ XPS analysis of Pd@ZnO-WO_3 NFs in the vicinity of Pd 3*d* (c) in air and (d) in toluene after 5 cycle sensing measurement toward 1 ppm of toluene at 350 °C.

CONCLUSIONS

In this work, M@MO complex catalysts, derived from ZIF-8 templates, were effectively incorporated into 1-D SMO NFs via electrospinning. Dual heterogeneous multijunctions were

DOI: 10.1021/jacs.6b09167
J. Am. Chem. Soc. 2016, 138, 13431−13437

thereby created within the 1-D composite NFs by the formation of Pd−ZnO and ZnO−WO_3 interfaces. The synthesized Pd@ZnO−WO_3 NFs exhibited high sensitivity toluene response (R_{air}/R_{gas} = 4.37 to 100 ppb) at 350 °C. Moreover, Pd@ZnO−WO_3 NFs showed reduced response time and superior selectivity. These results demonstrate that the MOF driven M@MO complex catalyst-loaded SMO NFs represent a new catalyst platform for the development of highly sensitive and selective chemical gas sensors. Furthermore, we expect that the proposed concept relating to utilizing MOF-assisted M@MO complex catalyst loading on SMO NFs can be applicable to other key technologies relying on highly active catalysts, such as Li−air batteries and hydrogen generation.

EXPERIMENTAL SECTION

Starting Materials. Polyvinylpyrrolidone (PVP, $M_w \approx 1\,300\,000$ g/mol), 2-methylimidazole (Hmin, 99.0%), and sodium borohydride ($NaBH_4$, 96%) were purchased from Aldrich. Zinc nitrate hexahydrate ($[Zn(NO_3)_2{\cdot}6H_2O]$, 98%), ammonium metatungstate hydrate (AMH, $[(NH_4)_6H_2W_{12}O_{40}{\cdot}xH_2O]$), methanol (MeOH, 99.9%), and potassium tetrachloropalladate(II) (K_2PdCl_4) were purchased from Sigma-Aldrich. All chemicals were used without further purification.

Synthesis of Pd@ZIF-8. ZIF-8 was synthesized by mixing zinc precursors and Hmin in MeOH. 2.933 g of $Zn(NO_3)_2{\cdot}6H_2O$ and 6.489 g of Hmin were dissolved separately in 200 mL MeOH. Then, a $Zn(NO_3)_2{\cdot}6H_2O$ solution was rapidly added into a solution of Hmin under magnetic stirring for 1 h at room temperature. The milky dispersion mixtures were dried at 50 °C in air, and purified by centrifugation and washing with ethanol. After purification, 40 mg of ZIF-8 was dispersed in 1 mL deionized water (DI-water). Ten mg of K_2PdCl_4 was added into a ZIF-8 dispersion solution under stirring with magnetic bar during 1 h, then Pd metal ions in the cavity of ZIF-8 were reduced by $NaBH_4$ solution (1.5 mg/mL). Lastly, as-prepared Pd@ZIF-8 suspension was purified by centrifugation and washing with DI-water and dispersed in 3 mL of DI-water.

Synthesis of Pd@ZnO−WO_3 NFs. Pd@ZnO−WO_3 NFs were prepared by electrospinning, followed by a calcination step. 0.4 g of AMH and 0.5 g of PVP were dissolved in DI-water solution for electrospinning. The Pd@ZIF-8 suspension was added to the electrospinning solution, followed by the electrospinning solution being continuously stirred at room temperature for 5 h. The electrospinning was conducted with the prepared solution at a feeding rate of 0.1 mL/min using a syringe pump at 25 °C with 30% RH. During electrospinning, high voltage (16 kV, DC) and distance (15 cm) were maintained between the tip of the syringe needle and the stainless steel foil collector. The as-spun Pd@ZIF-8 loaded AMH/PVP composite NFs were calcined at 500 °C for 1 h in air atmosphere with a heating rate of 4 °C/min.

Gas Sensor Measurements. Sensing characteristics were investigated within the temperature range of 300−450 °C toward various volatile organic compounds (VOCs) such as toluene, acetone, ammonia, hydrogen sulfide, ethanol, and nitrogen monoxide. After the sensors were stabilized by baseline air injection for 10 min, the analyte gas was injected for 10 min with a concentration ranging from 100 ppb to 5 ppm. The sensing measurements were conducted in a highly humid atmosphere (90% RH), similar to human exhaled breath. The relative gas responses (R_{air}/R_{gas} to reducing gas, R_{gas}/R_{air} to oxidizing gas) were evaluated by monitoring the resistance changes using a data acquisition system (34972, Agilent). The sensor temperatures were controlled by applying a specified voltage to the sensor Pt microheaters using a DC power supply (E3647A, Agilent).

Further detailed experimental procedures and characterization are described in the Supporting Information.

ASSOCIATED CONTENT

Supporting Information

The Supporting Information is available free of charge on the ACS Publications website at DOI: 10.1021/jacs.6b09167.

Experimental details, additional characterizations, and supporting table (PDF)

AUTHOR INFORMATION

Corresponding Author

*idkim@kaist.ac.kr

Notes

The authors declare no competing financial interest.

ACKNOWLEDGMENTS

This work was supported by the National Research Foundation (NRF) of Korea grant funded by the Ministry of Science, ICT and Future Planning (NRF-2015R1A2A1A16074901). This work was also supported by Wearable Platform Materials Technology Center (WMC) (NRF-2016R1A5A1009926) and Korea CCS R&D Center (KCRC) (NRF-2014M1A8A1049303) grant funded by the NRF of Korea grant of the Korea government (Ministry of Science, ICT and Future Planning). HLT's contribution to this work was supported in part by the MRSEC Program of the National Science Foundation under award number DMR−1419807.

REFERENCES

(1) (a) Kitagawa, S.; Kitaura, R.; Noro, S. *Angew. Chem., Int. Ed.* **2004**, *43*, 2334. (b) Eddaoudi, M.; Kim, J.; Rosi, N.; Vodak, D.; Wachter, J.; O'Keeffe, M.; Yaghi, O. M. *Proc. Natl. Acad. Sci. U. S. A.* **2002**, *295*, 4692. (c) Furukawa, H.; Cordova, K. E.; O'Keeffe, M.; Yaghi, O. M. *Science* **2013**, *341*, 974.

(2) (a) Murray, L. J.; Dinca, M.; Long, J. R. *Chem. Soc. Rev.* **2009**, *38*, 1294. (b) Rosi, N. L.; Eckert, J.; Eddaoudi, M.; Vodak, D. T.; Kim, J.; O'Keeffe, M.; Yaghi, O. M. *Science* **2003**, *300*, 1127.

(3) (a) Lee, J.; Farha, O. K.; Roberts, J.; Scheidt, K. A.; Nguyen, S. T.; Hupp, J. T. *Chem. Soc. Rev.* **2009**, *38*, 1450−1459. (b) Ren, Y. Q.; Chia, G. H.; Gao, Z. Q. *Nano Today* **2013**, *8*, 577.

(4) Yanai, N.; Kitayama, K.; Hijikata, Y.; Sato, H.; Matsuda, R.; Kubota, Y.; Takata, M.; Mizuno, M.; Uemura, T.; Kitagawa, S. *Nat. Mater.* **2011**, *10*, 787. (b) Kreno, L. E.; Leong, K.; Farha, O. K.; Allendorf, M.; Van Duyne, R. P.; Hupp, J. T. *Chem. Rev.* **2012**, *112*, 1105.

(5) (a) Horcajada, P.; Gref, R.; Baati, T.; Allan, P. K.; Maurin, G.; Couvreur, P.; Ferey, G.; Morris, R. E.; Serre, C. *Chem. Rev.* **2012**, *112*, 1232. (b) Horcajada, P.; Chalati, T.; Serre, C.; Gillet, B.; Sebrie, C.; Baati, T.; Eubank, J. F.; Heurtaux, D.; Clayette, P.; Kreuz, C.; Chang, J. S.; Hwang, Y. K.; Marsaud, V.; Bories, P. N.; Cynober, L.; Gil, S.; Ferey, G.; Couvreur, P.; Gref, R. *Nat. Mater.* **2010**, *9*, 172.

(6) (a) Hermes, S.; Schroter, M. K.; Schmid, R.; Khodeir, L.; Muhler, M.; Tissler, A.; Fischer, R. W.; Fischer, R. A. *Angew. Chem., Int. Ed.* **2005**, *44*, 6237. (b) Lu, G.; Li, S. Z.; Guo, Z.; Farha, O. K.; Hauser, B. G.; Qi, X. Y.; Wang, Y.; Wang, X.; Han, S. Y.; Liu, X. G.; DuChene, J. S.; Zhang, H.; Zhang, Q. C.; Chen, X. D.; Ma, J.; Loo, S. C. J.; Wei, W. D.; Yang, Y. H.; Hupp, J. T.; Huo, F. W. *Nat. Chem.* **2012**, *4*, 310. (c) Jiang, H. L.; Akita, T.; Ishida, T.; Haruta, M.; Xu, Q. *J. Am. Chem. Soc.* **2011**, *133*, 1304. (d) Zhang, W.; Liu, Y.; Lu, G.; Wang, Y.; Li, S.; Cui, C.; Wu, J.; Xu, Z.; Tian, D.; DuChene, J. S.; Wei, W. D.; Chen, H.; Yang, Y.; Huo, F. *Adv. Mater.* **2015**, *27*, 2923.

(7) (a) Choi, K. M.; Na, K.; Somorjai, G. A.; Yaghi, O. M. *J. Am. Chem. Soc.* **2015**, *137*, 7810. (b) Yan, J. M.; Wang, Z. L.; Gu, L.; Li, S. J.; Wang, H. L.; Zheng, W. T.; Jiang, Q. *Adv. Energy Mater.* **2015**, *5*, 1500107. (c) Chen, Y. Z.; Zhou, Y. X.; Wang, H. W.; Lu, J. L.; Uchida, T.; Xu, Q.; Yu, S. H.; Jiang, H. L. *ACS Catal.* **2015**, *5*, 2062.

(8) (a) Rai, P.; Majhi, S. M.; Yu, Y.-T.; Lee, J. H. *RSC Adv.* **2015**, *5*, 76229. (b) Lee, J. H. *Sens. Actuators, B* **2009**, *140*, 319−336. (c) Righettoni, M.; Amann, A.; Partsinis, S. E. *Mater. Today* **2015**, *18*, 163.
(9) (a) Wang, C.; Yin, L.; Zhang, L.; Xiang, D.; Gao, R. *Sensors* **2010**, *10*, 2088. (b) Kim, H. J.; Lee, J. H. *Sens. Actuators, B* **2014**, *192*, 607.
(10) (a) Ma, Q.; Yu, W.; Dong, X.; Wang, J.; Liu, G. *Adv. Funct. Mater.* **2015**, *25*, 2436. (b) Ma, Q.; Yu, W.; Dong, X.; Wang, J.; Liu, G. *Nanoscale* **2014**, *6*, 2945. (c) Greiner, A.; Wendorff, J. H. *Angew. Chem., Int. Ed.* **2007**, *46*, 5670.
(11) (a) Ostermann, R.; Cravillon, J.; Weidmann, C. *Chem. Commun.* **2011**, *47*, 442. (b) Wu, Y. N.; Li, F. T.; Liu, H. M.; Zhu, W.; Teng, M. M.; Jiang, Y.; Li, W. N.; Xu, D.; He, D. H.; Hannam, P.; Li, G. T. *J. Mater. Chem.* **2012**, *22*, 16971. (c) Quiros, J.; Boltes, K.; Aguado, S.; de Villoria, R. G.; Vilatela, J. J.; Rosal, R. *Chem. Eng. J.* **2015**, *262*, 189.
(12) (a) Kim, N. H.; Choi, S. J.; Yang, D. J.; Bae, J.; Park, J.; Kim, I. D. *Sens. Actuators, B* **2014**, *193*, 574. (b) Choi, S. J.; Kim, S. J.; Koo, W. T.; Cho, H. J.; Kim, I. D. *Chem. Commun.* **2015**, *51*, 2609. (c) Lou, Z.; Deng, J.; Wang, L. J.; Fei, T.; Zhang, T. *Sens. Actuators, B* **2013**, *176*, 323.
(13) Park, K. S.; Ni, Z.; Cote, A. P.; Choi, J. Y.; Huang, R. D.; Uribe-Romo, F. J.; Chae, H. K.; O'Keeffe, M.; Yaghi, O. M. *Proc. Natl. Acad. Sci. U. S. A.* **2006**, *103*, 10186.
(14) Sorribas, S.; Zornoza, B.; Tellez, C.; Coronas, J. *Chem. Commun.* **2012**, *48*, 9388. (b) Xie, J. K.; Yan, N. Q.; Liu, F.; Qu, Z.; Yang, S. J.; Liu, P. *Front. Environ. Sci. Eng.* **2014**, *8*, 162. (c) Schejn, A.; Mazet, T.; Falk, V.; Balan, L.; Aranda, L.; Medjahdi, G.; Schneider, R. *Dalton Trans.* **2015**, *44*, 10136.
(15) Newsome, T. E.; Olesik, S. V. *J. Appl. Polym. Sci.* **2014**, *131*, 40966.
(16) Choi, S. J.; Choi, C.; Kim, S. J.; Cho, H. J.; Hakim, M.; Jeon, S.; Kim, I. D. *Sci. Rep.* **2015**, *5*, 8067.
(17) Wang, G. M.; Ling, Y. C.; Wang, H. Y.; Yang, X. Y.; Wang, C. C.; Zhang, J. Z.; Li, Y. *Energy Environ. Sci.* **2012**, *5*, 6180.
(18) Wu, H. Y.; Xu, M.; Da, P. M.; Li, W. J.; Jia, D. S.; Zheng, G. F. *Phys. Chem. Chem. Phys.* **2013**, *15*, 16138.
(19) Li, C. C.; Yin, X. M.; Li, Q. H.; Wang, T. H. *CrystEngComm* **2011**, *13*, 1557.
(20) Koo, W. T.; Choi, S. J.; Kim, N. H.; Jang, J. S.; Kim, I. D. *Sens. Actuators, B* **2016**, *223*, 301.
(21) Peng, G.; Tisch, U.; Adams, O.; Hakim, M.; Shehada, N.; Broza, Y. Y.; Billan, S.; Abdah-Bortnyak, R.; Kuten, A.; Haick, H. *Nat. Nanotechnol.* **2009**, *4*, 669.
(22) Kim, I. D.; Rothschild, A.; Tuller, H. L. *Acta Mater.* **2013**, *61*, 974.
(23) (a) Kim, H. R.; Haensch, A.; Kim, I. D.; Barsan, N.; Weimar, U.; Lee, J. H. *Adv. Funct. Mater.* **2011**, *21*, 4456. (b) Ma, N.; Suematsu, K.; Yuasa, M.; Kida, T.; Shimanoe, K. *ACS Appl. Mater. Interfaces* **2015**, *7*, 5863.
(24) Miekisch, W.; Schubert, J. K.; Noeldge-Schomburg, G. F. E. *Clin. Chim. Acta* **2004**, *347*, 25.
(25) Yamazoe, N.; Sakai, G.; Shimanoe, K. *Catal. Surv. Asia* **2003**, *7*, 63.
(26) (a) Li, D.; Haneda, H. *J. Photochem. Photobiol., A* **2003**, *160*, 203. (b) Miller, D. R.; Akbar, S. A.; Morris, P. A. *Sens. Actuators, B* **2014**, *204*, 250. (c) Tao, C.; Ruan, S. P.; Xie, G. H.; Kong, X. Z.; Shen, L.; Meng, F. X.; Liu, C. X.; Zhang, X. D.; Dong, W.; Chen, W. Y. *Appl. Phys. Lett.* **2009**, *94*, 043311. (d) Katoch, A.; Kim, J. H.; Kwon, Y. J.; Kim, H. W.; Kim, S. S. *ACS Appl. Mater. Interfaces* **2015**, *7*, 11351.
(27) Acharyya, D.; Huang, K. Y.; Chattopadhyay, P. P.; Ho, M. S.; Fecht, H. J.; Bhattacharyya, P. *Analyst* **2016**, *141*, 2977.
(28) (a) Song, X. F.; Zhang, D. J.; Fan, M. *Appl. Surf. Sci.* **2009**, *255*, 7343. (b) Ding, X. H.; Zeng, D. W.; Zhang, S. P.; Xie, C. S. *Sens. Actuators, B* **2011**, *155*, 86.
(29) (a) Wang, C. Y.; Hong, Z. S.; Wu, R. J. *Phys. E* **2015**, *69*, 191. (b) Hu, J.; Gao, F. Q.; Sang, S. B.; Li, P. W.; Deng, X.; Zhang, W. D.; Chen, Y.; Lian, K. *J. Mater. Sci.* **2015**, *50*, 1935.

DOI: 10.1021/jacs.6b09167
J. Am. Chem. Soc. 2016, 138, 13431−13437